Geometrically Tunable Beamed Light Emission from a Quantum-Dot Ensemble Near a Gradient Metasurface

Xiaowei Wang, Yuyu Li, Reyhaneh Toufanian, Leonard C. Kogos, Allison M. Dennis, and Roberto Paiella*

Optical metasurfaces have been widely investigated in recent years as a means to tailor the wavefronts of externally incident light for passive device applications. At the same time, their use in active optoelectronic devices such as light emitters is far less established. This work explores their ability to control the radiation properties of a nearby continuous ensemble of randomly oriented incoherent dipole sources via near-field interactions. Specifically, a film of colloidal quantum dots is deposited on a plasmonic metasurface consisting of a 1D array of metallic nanoantennas on a metal film. The array is designed to introduce a linear phase profile upon reflection, and a bi-periodic nanoparticle arrangement is introduced to ensure adequate sampling of the desired phase gradient. Highly directional radiation patterns are correspondingly obtained from the quantum dots at an enhanced emission rate. The underlying radiation mechanism involves the near-field excitation of surface plasmon polaritons at the metal film, and their selective diffractive scattering by the metasurface into well-collimated beams along predetermined geometrically tunable directions. These results underscore the distinctive ability of metasurfaces to control radiation properties directly at the source level, which is technologically significant for the continued miniaturization and large-scale integration of optoelectronic devices.

1. Introduction

Light-emission engineering is a major topic of fundamental and applied research in photonics. The key underlying idea is the ability to control spontaneous emission by an arbitrary radiation source via modification of its local dielectric environment. This idea is well established in the context of surface-enhanced

fluorescence as a way to increase emission rates.[1] A wide range of (nano) photonic and plasmonic structures have also been employed for the same purpose, including optical cavities[2,3] and nanoantennas.[4–15] A common feature of all these systems is the presence of resonant modes featuring hot spots of highly enhanced optical field intensity. When a radiation source (e.g., an oscillating electric dipole) is located at such hot spots, its emission rate is increased by an amount proportional to the local field-intensity enhancement. Under these conditions, the output light mostly originates from the excitation and subsequent radiative decay of the underlying resonant modes. As a result, its far-field properties (including directionality and polarization) are to a large extent determined by the nature of these resonances, rather than the original dipole sources. Suitably designed optical cavities and nanoantennas can therefore be used to enhance emission rates and at the same time control the far-field pattern of the output radiation. Significant additional degrees of freedom to engineer the same functionalities are also provided by tailored arrays of these optical elements,[16] including deterministic aperiodic arrangements.[17]

In the context of beamed light emission, several remarkable demonstrations of this basic idea have been reported in recent years, but mainly limited to highly localized nanoscale sources (e.g., single quantum dots (QDs), molecules, nanowires), carefully positioned to optimally excite the resonant modes of a nanoantenna.[18–21] For extended-area light emitters (i.e., planar samples with microscale lateral dimensions, as used in typical optoelectronic devices), directional radiation patterns can be obtained with periodic structures such as photonic[22–25] or plasmonic crystals.[26–28] However, so far this approach has been largely limited to the generation of symmetric radiation patterns (with respect to the sample surface normal), due to identical contributions from equal and opposite diffraction orders. Asymmetric unidirectional light emission can be implemented by tailoring the shape of the unit cells of the periodic structure to introduce asymmetry in its diffraction response. Suitable geometries recently explored for this purpose include triangular nanoantennas[29] and asymmetric nanoparticle (NP) dimers.[30]

Dr. X. Wang, Y. Li, Dr. L. C. Kogos, Prof. R. Paiella
Department of Electrical and Computer Engineering
and Photonics Center
Boston University
8 Saint Mary's Street, Boston, MA 02215, USA
E-mail: rpaiella@bu.edu
R. Toufanian, Prof. A. M. Dennis
Department of Biomedical Engineering and Division of Materials
Science and Engineering
Boston University
8 St. Mary's St., Boston, MA 02215, USA

The ORCID identification number(s) for the author(s) of this article can be found under https://doi.org/10.1002/adom.201901951.

**ADVANCED
SCIENCE NEWS**
www.advancedsciencenews.com

**ADVANCED
OPTICAL
MATERIALS**
www.advopticalmat.de

Here we consider instead the control of spontaneous emission using more complex gradient metasurfaces (GMSs), that is, planar arrays of subwavelength nanoantennas designed to introduce any desired phase profile in their reflected and/or transmitted light. These systems provide a powerful tool to shape the wavefronts of externally incident light, as a way to enable a wide range of photonic device functionalities (including lenses, polarization devices, and holograms) in an ultrathin flat format.[31–34] Recent theoretical work has shown that the same metasurfaces can also be used to tailor light emission by an oscillating dipole in their near-field vicinity, by scattering the evanescent components of the dipole field into radiation in a highly controllable fashion.[35] In particular, the calculations presented in that work considered a generic GMS featuring a linearly graded reflection phase profile, described with a homogenized continuum model. Correspondingly, it was found that highly directional and polarized radiation can be obtained at an enhanced emission rate from a nearby ensemble of incoherent isotropic sources. The resulting direction of peak emission is determined by the reflection phase gradient and therefore can be tuned by design by varying the GMS geometrical parameters.

In the present work, these ideas are demonstrated experimentally using a continuous distribution of colloidal QDs deposited on a reflective GMS consisting of a 1D array of rectangular plasmonic NPs on a metal film. The NPs are designed to produce a discretized version of the desired linear phase profile, and a bi-periodic arrangement (with different numbers of NPs in alternating periods) is introduced to suppress all spurious orders of diffraction that would otherwise produce multiple output beams. Asymmetric unidirectional light emission is obtained from the QDs at geometrically tunable polar angles ranging from about 10° to 50°. These results highlight the unique promise of GMSs in the context of surface-enhanced light emission, as a means to efficiently extract light from a planar active layer and radiate it in a desired direction, without the use of any external bulk optical elements. This capability is technologically significant for the continued miniaturization of optoelectronic components toward ever increasing levels of device functionality and system integration.

2. Results and Discussion

The specific GMS platform employed in this work is illustrated schematically in **Figure 1**. The individual nanoantennas consist of rectangular Au NPs placed on a SiO$_2$ layer of highly subwavelength thickness supported by an optically thick Au film. The entire structure is capped with a polymer layer containing a planar ensemble of light-emitting QDs at a near-field distance from the GMS (red dots in Figure 1). The NPs can be regarded as infinitely long in the y direction, whereas their width in the x direction (L_x) determines their reflection phase for x-polarized incident light.[36,37] The array is designed so that this phase shift varies linearly with position along the x direction with a predetermined slope ξ. Under these conditions, x-polarized externally incident light of in-plane wavevector **p** is preferentially scattered into a reflected wave of in-plane wavevector $\mathbf{p} + \xi\hat{x}$, leading to anomalous (non-specular) reflection.[36] The GMS is
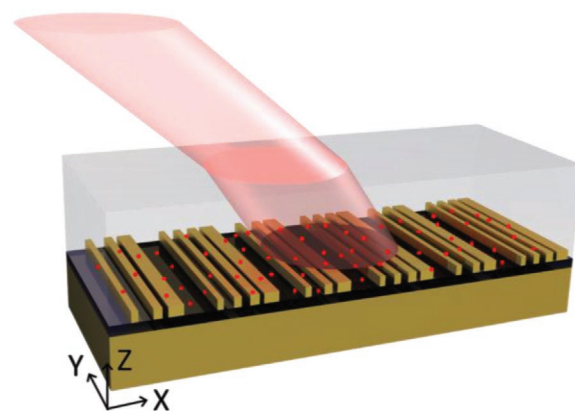

Figure 1. Gradient metasurface for directional light emission. Schematic illustration of the device structure developed in this work, including its directional radiation output. From bottom to top, the device consists of a Au film, a SiO$_2$ layer, an array of rectangular Au NPs, and a polymer cap layer. The red dots indicate the light-emitting QDs embedded in the polymer.

therefore functionally equivalent to a reflective blazed diffraction grating where all orders of diffraction are completely suppressed except for the positive first order, but with the distinct advantages of ultrathin flat geometry and simple fabrication involving only planar processing steps.

When a radiating dipole is located in the near-field zone of a metal–dielectric interface (such as the QDs near the Au/SiO$_2$ boundary in Figure 1), its evanescent field components can excite surface plasmon polaritons (SPPs) at the interface through a resonant phase-matched interaction. In fact, because of the strong near-field confinement of SPPs, this process can occur with particularly high probability rate, at the expense of all other possible dipole relaxation mechanisms, including direct light emission in the far-field.[1] In the GMS under study, the excited SPPs are then scattered by the NP array into radiation through the positive first-order diffraction process just described. As a result, the output light of the combined dipole-GMS system predominantly consists of plane-wave components of in-plane wavevectors $\mathbf{k}_{\text{SPP}} + \xi\hat{x}$, leading to a highly directional radiation pattern determined by the SPP wavevectors $\mathbf{k}_{\text{SPP}}$ and the GMS phase gradient ξ. The resulting beamed light emission can also be expected to be linearly polarized along the direction perpendicular to the NPs, since the GMS is most effective at scattering SPPs propagating at small angles with respective to the x axis, whose in-plane field component is also along the x direction.

The polar angle θ_{cap} of peak emission inside the polymer cap layer can be computed from the diffraction condition based on the arguments just presented. On the x–z plane of Figure 1 (the plane perpendicular to the NPs), the resulting formula is simply

$$\frac{2\pi}{\lambda_0} n_{\text{cap}} \sin\theta_{\text{cap}} = -\frac{2\pi}{\lambda_0} n_{\text{SPP}} + \xi \qquad (1)$$

where λ_0 is the free-space emission wavelength, $n_{\text{cap}} \approx 1.48$ is the polymer refractive index, and $n_{\text{SPP}} = k_{\text{SPP}}\lambda_0/2\pi$ is the SPP effective index. After the diffraction process described by this
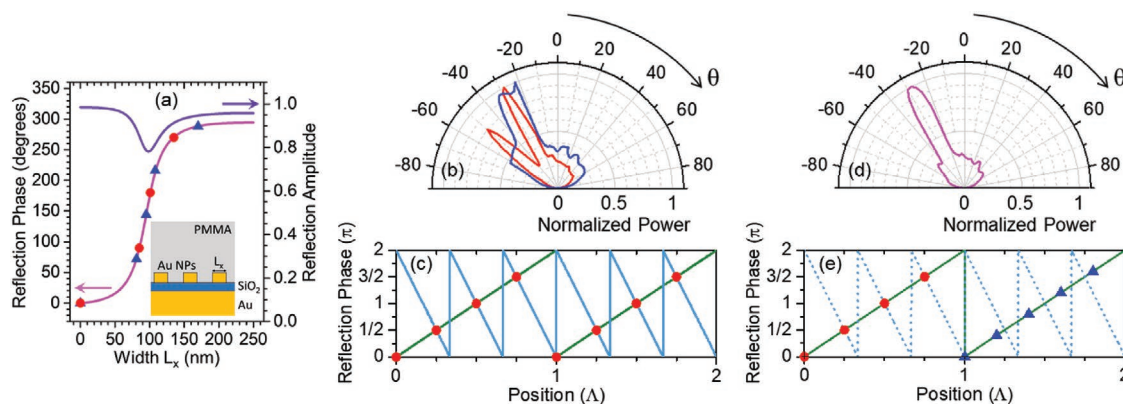
ADVANCED
SCIENCE NEWS
www.advancedsciencenews.com

ADVANCED
OPTICAL
MATERIALS
www.advopticalmat.de

Figure 2. Metasurface design. a) Calculated reflection phase (magenta trace) and amplitude (violet trace) of the individual nanoantennas used in this work, plotted as a function of NP width along the x direction. The circles and triangles indicate a set of 4 and 5 NP widths, respectively, with equally spaced reflection-phase values sampling the entire 2π range. The device structure used in these calculations is shown in the inset. b) Calculated far-field radiation patterns of a planar ensemble of light-emitting dipoles near a GMS with period $\Lambda = 860$ nm for different numbers of equally spaced NPs per unit cell: $N = 4$ (red trace) and 5 (blue trace). The free-space emission wavelength is $\lambda_0 = 800$ nm, and the dipoles are located 15 nm above the top of the NPs. c) Symbols: NP reflection phase versus center position for the $N = 4$ design of (b). Green trace: linear phase profile with slope $+2\pi/\Lambda$. Light blue trace: linear phase profile with slope $-6\pi/\Lambda$. d,e) Same as (b) and (c), respectively, for a GMS based on the bi-periodic design illustrated in Figure 1, with the two alternating unit cells containing 4 and 5 NPs over the same length $\Lambda = 860$ nm.

equation, the output light is finally refracted at the top surface of the cap layer, so that the beaming angle θ_0 in the free space above is related to θ_{cap} by Snell's law, that is, $n_{cap}\sin \theta_{cap} = \sin \theta_0$. In passing, we note that the polymer layer should also be sufficiently thick on the scale of the emission wavelength so that all of its dielectric-guided modes are relatively delocalized. As a result, these modes do not compete significantly with the SPPs for the QD emission, which is important in order to avoid the appearance of additional peaks in the radiation pattern (at angles given by the diffraction formula of Equation (1) with n_{SPP} replaced by the guided-modes effective indexes).

To illustrate the metasurface design, **Figure 2**a shows the reflection phase of its individual nanoantennas as a function of NP width L_x, as computed by finite difference time domain (FDTD) simulations for x-polarized light at normal incidence with $\lambda_0 = 800$ nm. The SiO$_2$ film thickness and Au NP height used in these calculations and throughout this work are both equal to 30 nm. As shown by these simulation results, a reasonably large fraction ($\approx$80%) of the entire 2π phase space can be covered by varying L_x from 0 to about 250 nm (specifically, through the coupling between the NP and its dipolar image in the metal film[36,37]). At the same time, the reflection amplitude remains relatively high (>78%) across the entire range considered. A discretized version of the desired linear phase profile can then be implemented with a periodic array of such nanoantennas, where each repeat unit contains a set of equally spaced NPs of different widths corresponding to equally spaced reflection-phase values across the full 2π range. In particular, if the separation between neighboring NPs is Λ/N (where Λ is the array period and N is the number of NPs per unit cell) and their phase values differ by $\Delta\phi = 2\pi/N$, a linear reflection-phase profile with gradient $\xi = 2\pi/\Lambda$ is obtained along the x direction. The triangles (circles) in Figure 2a show a suitable set of $N = 5$ ($N = 4$) NP widths with $\Delta\phi = 2\pi/5$ ($\Delta\phi = \pi/2$). Both sets include a NP of zero width, equivalent to a missing NP in the array. This choice is particularly convenient from a practical standpoint because it eliminates the need to fabricate ultra-small

($\lesssim$50 nm) NPs, and therefore has been adopted in all devices described below.

With this general approach, we have developed five representative GMS structures designed to produce directional light emission peaked at five different angles θ_0, ranging from about $-10°$ to $-50°$ in steps of $10°$; the negative signs here simply indicate that the in-plane wavevector of the output light is in the opposite direction relative to the GMS phase gradient. The design emission wavelength is 800 nm, determined by the fluorescence properties of the CdTe/ZnS QDs used in the experimental samples. The required GMS period Λ for any desired beaming angle θ_0 increases with increasing $|\theta_0|$ and can be determined from Equation (1) combined with the relation $\xi = 2\pi/\Lambda$ and Snell's law. Given Λ, an important design parameter is the number N of NPs per repeat unit, and the optimal choice is governed by two conflicting requirements: 1) N must be sufficiently large so that all undesired orders of diffraction are suppressed; 2) the inter-NP spacing Λ/N must be large enough to avoid near-field interactions between neighboring NPs, which can degrade the expected linear phase profile.

The resulting tradeoff is illustrated in Figure 2b–e for a GMS period Λ of 860 nm, corresponding to an angle of peak emission in the polymer cap layer $\theta_{cap} = -28°$. The red trace in Figure 2b shows the QD far-field radiation pattern (on the x–z plane inside the polymer) obtained with a GMS where each period contains the 4-NP set of Figure 2a, as computed by FDTD simulations based on the principle of reciprocity (see Section 4 for more details). In addition to the desired beam at the target design angle of $-28°$, a second peak of comparable magnitude is obtained at an angle of $-50°$, corresponding to negative third-order diffraction of SPPs. The origin of this additional peak is elucidated in Figure 2c, where the circles indicate the reflection-phase values of the NPs used in this device plotted as a function of their center position along the x direction. As shown in the figure, these circles provide a discretized version of a linear phase profile with slope $+2\pi/\Lambda$ (green trace) as well as $-6\pi/\Lambda$ (light blue trace), which implies that the NP array can scatter incident light

**ADVANCED
SCIENCE NEWS**
www.advancedsciencenews.com

**ADVANCED
OPTICAL
MATERIALS**
www.advopticalmat.de

by both positive first-order and negative third-order diffraction. In fact, similar arguments indicate that, if N equally spaced NPs per unit cell are used to approximate a linear phase profile, one every N diffraction orders is correspondingly allowed (i.e., $q = +1, 1 - N, 1 + N, 1 - 2N, 1 + 2N$, etc.). A peak in the far-field pattern is therefore obtained for any such diffraction order that can scatter SPPs into radiative waves, that is, for $q = +1$ and -3 in Figure 2b. In contrast, if 5 NPs per period are employed (again for $\Lambda = 860$ nm), only one radiation peak is expected, since SPP scattering by all allowed diffraction orders except for $q = +1$ is evanescent in this case. At the same time, however, the inter-NP spacing (172 nm center-to-center) is sufficiently small that the reflection phase of each individual NP is strongly affected by near-field interactions with its nearest neighbors, by an amount that depends on their respective widths. As a result, the far-field radiation pattern is significantly degraded, as illustrated by the blue trace in Figure 2b, where a relatively large background due to incomplete suppression of multiple undesired diffraction orders is observed.

This tradeoff can be addressed using a periodic repetition of two alternating unit cells with the same length Λ but different numbers of NPs, as shown schematically in Figure 1. To illustrate the resulting device performance, Figure 2d shows the calculated far-field radiation pattern produced by a GMS based on this bi-periodic arrangement, where the two alternating unit cells are identical to those of the two structures of Figure 2b. A single peak at the target beaming angle of $-28°$ is obtained over a rather low background. The suppression of spurious diffraction peaks can be understood from the phase versus position diagram of Figure 2e and related considerations, which indicate that only one every $4 \times 5 = 20$ diffraction orders (with respect to the period Λ) is allowed in this structure. At the same time, the presence of reasonably large inter-NP spacings in at least half of the array surface is sufficient to avoid the degradation in overall shape of the radiation pattern observed in the blue trace of Figure 2b. In passing, we note that an alternative approach for the design of suitable GMSs is a non-periodic array of equally spaced NPs with continuously changing widths sampling the desired linear phase profile. However, the latter approach requires a wider range of reflection phase shifts, including values outside of the range covered by the individual nanoantennas (see Figure 2a), which can also degrade the resulting radiation patterns as well as complicate the GMS numerical design and fabrication.

The design parameters of the five GMSs developed in this work are listed in **Table 1**, including their array period Λ, number of NPs per unit cell N, and individual NP widths. For the two devices designed to produce beamed light emission

peaked at $\theta_0 = -30°$ and $-50°$, a single-period arrangement with 4 and 5 NPs per unit cell, respectively, was found to be appropriate. The other three GMSs are based instead on the bi-periodic design strategy. For fixed N, the individual NP widths are determined from the phase map of Figure 2a. In some instances, these values (as well as the NP center positions) are then fine-tuned to compensate for near-field coupling effects in the GMS array, and therefore improve the suppression of undesired diffraction orders and the overall directionality of the output light. The beaming capabilities of all five devices are shown in **Figure 3**a–e, where we plot their calculated far-field radiation patterns in the free space above the polymer cap layer, for a planar ensemble of light-emitting dipoles located at a distance of 15 nm over the top of the NPs. Specifically, these color maps were obtained by averaging the results of several 3D FDTD simulations for a single dipole emitter at different positions and with different orientations (see Section 4 for more details). A highly directional radiation pattern is computed for each device, with most of the emission concentrated within a relatively narrow distribution of angles. The characteristic C-shape of these distributions is a direct signature of positive-first-order diffraction of SPPs into the radiation cone. The line cuts of all five radiation maps along their horizontal axes (i.e., the radiation patterns on the x–z plane) are plotted in Figure 3f, showing their respective polar angles of peak emission θ_0 varying from about $-10°$ to $-50°$.

In our experimental samples, the radiation sources consist of commercially available CdTe/ZnS QDs with a fluorescence spectrum peak at about 800 nm,[38] suspended in a solution of toluene and poly(lauryl methacrylate) (PLMA). The GMSs are fabricated by electron-beam lithography, with the Au and SiO_2 materials deposited by electron-beam evaporation and plasma-enhanced chemical vapor deposition (PECVD), respectively. A top-view scanning electron microscopy (SEM) image of a 630-nm-period array is shown in **Figure 4**a. The NPs are planarized with a thin layer (30 nm) of poly(methyl methacrylate) (PMMA) before deposition of the QD PLMA film (also about 30-nm thick), leading to a homogeneous distribution of randomly-oriented light emitters at a fixed subwavelength distance over the GMS. The resulting devices are finally capped with an optically thick (≈ 10 μm) additional layer of PMMA. In the optical measurements, the QD photoluminescence is excited with laser light at 405-nm wavelength, and the resulting far-field radiation patterns are measured with a Fourier microscopy setup including an objective lens with 0.95 numerical aperture and an optical filter with pass-band centered at 800 nm.

Figure 4 shows a set of data measured with a 630-nm-period GMS, including the unpolarized, x-polarized, and γ-polarized

Table 1. Design parameters of the five different devices developed in this work.

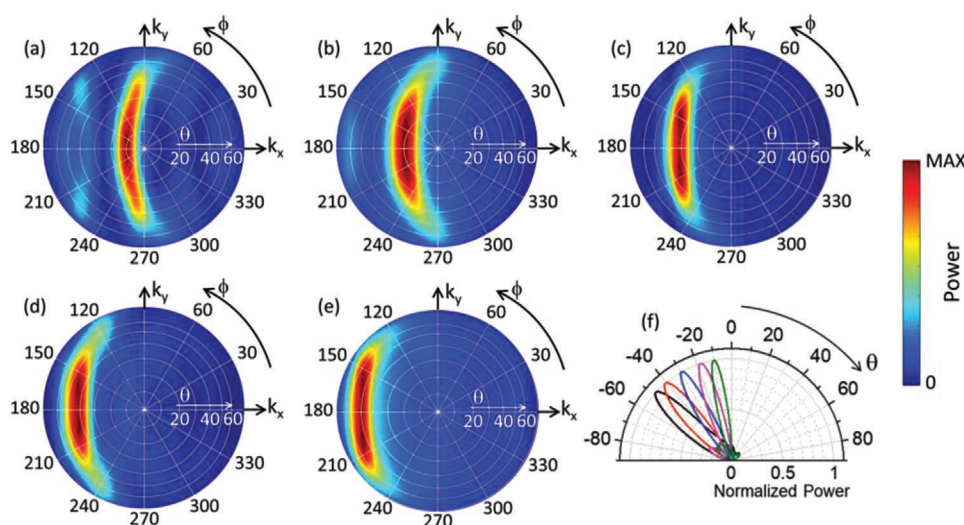| Peak emission angle in air [°]	Period of a single unit cell [nm]	Number of NPs in each unit cell used in design	NP width [nm]
−12	570	2, 3	[0, 101], [0, 98, 135]
−20	630	3, 4	[0, 84, 126], [0, 71, 93, 150]
−30	750	4	[0, 75, 95, 150]
−40	860	4, 5	[0, 76, 98, 174], [0, 71, 89, 112, 180]
−50	1000	5	[0, 71, 89, 112, 180]

Figure 3. FDTD simulation results. a–e) Calculated far-field radiation patterns of a planar ensemble of light-emitting dipoles near the GMSs of Table 1. In each color map, the radial distance from the origin corresponds to the polar emission angle, while the direction on the circle corresponds to the azimuthal angle. f) Line cuts of the same radiation patterns along their horizontal axis normalized to their peak value.

far-field radiation patterns (panels (b), (c), and (d), respectively) and their line cuts along the horizontal axis (panels (e)–(g)). A $\cos\theta$ normalization factor has been used to compute the latter traces from the raw data of the color maps, so as to produce a plot of optical power per unit solid angle versus polar emission angle (the radiation patterns measured with the Fourier microscopy setup correspond instead to radiance, or intensity per unit solid angle).[39] The expected C-shaped region of high emission is clearly observed in the unpolarized and x-polarized maps, with the corresponding line cuts featuring a narrow beam centered at $\theta_0 \approx -20°$ with a small divergence angle of 12° full-width at half maximum (FWHM) in panel (f). In contrast, no diffraction peaks are observed in the y-polarized map of panel (d), consistent with the polarization properties discussed above. Away from the C-shaped region, the x- and y-polarized signals are comparable in magnitude, and mostly originate from a radiation process where SPPs are excited by the QDs and then

scattered isotropically by roughness in the Au and SiO_2 films. Direct emission by the QDs into the far field also contributes to this unpolarized background, but it can be expected to be relatively weak compared to SPP emission because of the large SPP-field intensity at the locations of the QDs.[1] This conclusion is supported by the simulations of Figure 3, where film roughness is not included and a larger peak-to-background ratio is obtained compared to the experimental data.

Highly directional QD fluorescence is similarly obtained with all other GMS structures of Table 1, as shown by the x-polarized radiation patterns of **Figure 5**. The polar angles of peak emission of these devices range from −11° in Figure 5a to −57° in Figure 5d, clearly illustrating their geometrical tunability. In particular, these angles increase with increasing GMS period Λ as expected, although a slight difference from their simulated values of Table 1 is observed in some devices. This behavior can be attributed to deviations from the target values
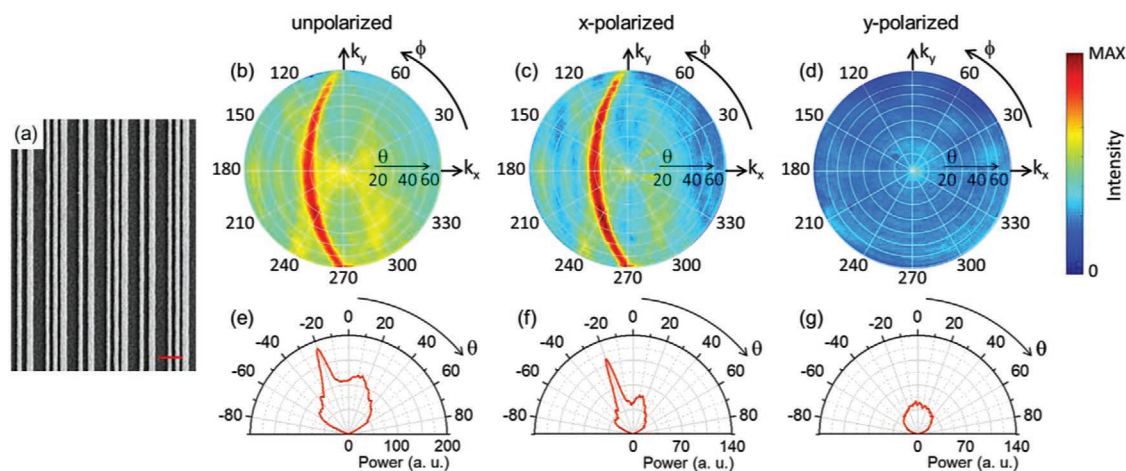

Figure 4. Measurement results for a GMS designed for peak emission at $\theta_0 = -20°$. a) Top-view SEM image. The scale bar is 500 nm. b–d) Unpolarized (b), x-polarized (c), and y-polarized (d) far-field radiation patterns of a planar ensemble of QDs in the near-field zone of the GMS. The same color scale is used in (c) and (d). e–g) Line cuts of the color maps of (b)–(d) along their horizontal axis, rescaled by a $\cos\theta$ normalization factor.
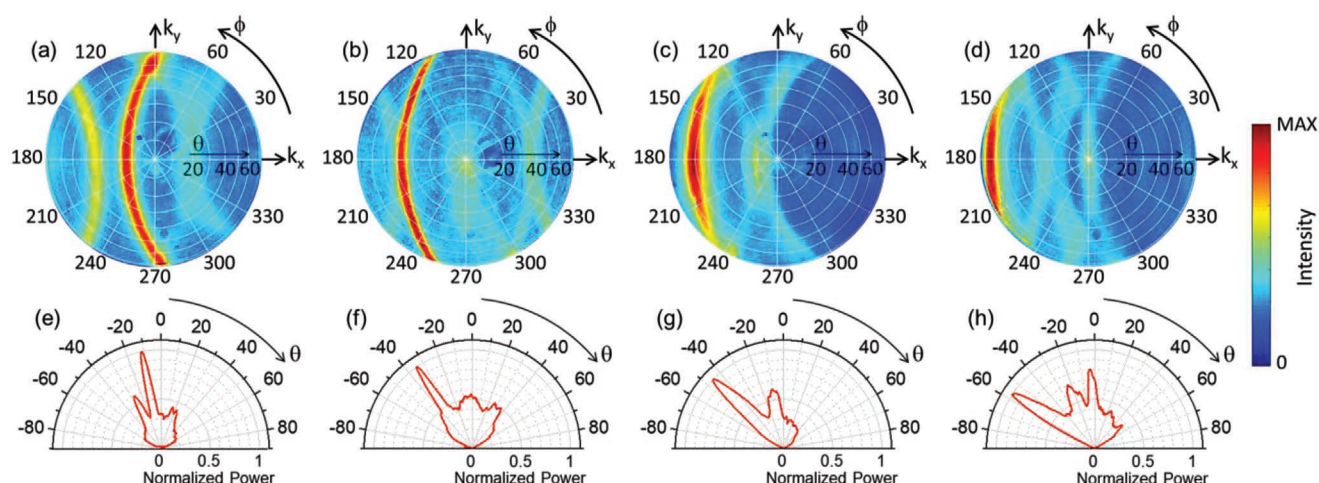
**ADVANCED
SCIENCE NEWS**
www.advancedsciencenews.com

**ADVANCED
OPTICAL
MATERIALS**
www.advopticalmat.de

Figure 5. Measurement results for several GMS designs of different period Λ. a–d) X-polarized far-field radiation patterns of a planar ensemble of QDs in the near-field zone of a GMS with $\Lambda = 570$ nm (a), 750 nm (b), 860 nm (c), and 1000 nm (d). e–h) Line cuts of the color maps of (a)–(d) along their horizontal axis, rescaled by a $\cos\theta$ normalization factor.

in some of the GMS geometrical parameters (e.g., the SiO$_2$ film thickness) that can cause variations in the SPP effective index of Equation (1). Additionally, some of the radiation patterns of Figure 5 show incomplete suppression of undesired diffraction orders leading to residual emission peaks, which are likely caused by fabrication inaccuracies in the NP widths. At the same time, the main output beam associated with positive first-order diffraction by the GMS is consistently found to be particularly pronounced and extremely narrow, with FWHM ranging from 9° in Figure 5e to 17° in Figure 5h. In fact, these measured divergence angles are even smaller than the theoretical values from Figure 3f, which vary from 12° to 21° in order of increasing GMS period. This discrepancy is attributed to approximations in the FDTD simulations, particularly related to apodization effects in the far-field transformations.

Finally, **Figure 6** presents a comparison of the x- and y-polarized radiation patterns measured with identical QD ensembles on a GMS (blue trace), on the underlying Au film without any NP array (black trace), and on an uncoated substrate consisting of an oxidized Si wafer (red trace). A Lambertian profile is obtained for both polarizations in the two samples without the GMS, with a uniform increase in output intensity in the

presence of the Au film. The latter behavior is related to several factors, including higher reflection by the Au film compared to the Si/SiO$_2$ substrate, increased QD emission rate through the near-field excitation of SPPs, and the interplay between SPP absorption via ohmic losses in the metal and scattering by surface roughness. In the presence of the GMS, the expected x-polarized diffraction peak is introduced over a Lambertian background that has essentially the same intensity as in the unpatterned Au-film sample. The key conclusion that emerges from this comparison is that the GMSs under study can not only reshape the radiation pattern of a nearby dipole source, but also increase the output power in the target directions of peak emission. The magnitude of this enhancement (about 4× in Figure 6a relative to the standard Si/SiO$_2$-substrate configuration) depends on the GMS properties as well as the internal quantum efficiency of the dipole sources.[35]

3. Conclusion

We have demonstrated a metasurface platform for the directional control of light emission from an arbitrary distribution of randomly-oriented incoherent radiation sources. The underlying operating principle involves the preferential excitation of guided waves (SPPs) via near-field interactions, and their selective scattering into predetermined directions by a periodic NP array designed to suppress all radiative diffraction orders except for one. In passing, we note that a related approach, where the guided waves are provided by a vertical resonant cavity, has been reported recently.[40] In the present work, highly directional radiation patterns are measured from colloidal QDs deposited on different GMSs, featuring pronounced emission beams with narrow divergence angles along geometrically tunable directions. These metasurfaces are compatible with planar active layers of arbitrary spatial extent, and therefore could be integrated with existing light-emitting device technologies for applications such as solid-state smart lighting, micro displays, structured illumination for computational imaging, and
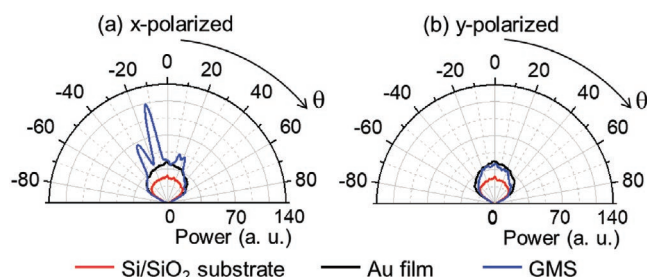

Figure 6. Comparison of the radiation patterns on the plane perpendicular to the NPs measured with identical QD ensembles on a GMS with $\Lambda = 570$ nm (blue trace), on the underlying Au film without any NP array (black trace), and on an uncoated substrate consisting of an oxidized Si wafer (red trace). Panels (a) and (b) show x- and y-polarized data, respectively.

**ADVANCED
SCIENCE NEWS**
www.advancedsciencenews.com

**ADVANCED
OPTICAL
MATERIALS**
www.advopticalmat.de

fluorescence sensing. The same operating principle could also be applied to the reverse device functionality (photodetection) for the development of angle-sensitive image sensors. More generally, similar metasurface devices could be envisioned for the direct emission of more complex radiation patterns, including for example focused beams and light with spin and/ or orbital angular momentum.

4. Experimental Section

Design Simulations: The directional metasurfaces presented in this work are designed via FDTD simulations with a commercial software package (FDTD Solutions by Lumerical). Initial design simulations consider a 2D structure (on the x–z plane of Figure 1), consisting of a unit cell of the GMS capped by a semi-infinite layer with refractive index of 1.48 (approximately equal to that of both PMMA and PLMA). Periodic boundary conditions are applied to the lateral boundaries of the simulation region, whereas perfectly matched layers (PMLs) are used in the top and bottom surfaces. The SiO_2 and Au layers are described with their complex permittivity functions from the built-in database of the FDTD software. The NP widths are selected as described above from the calculated plot of reflection phase versus width (Figure 2a), which is obtained from prior FDTD simulations based on an s-parameter extraction method. The expected radiation pattern is then evaluated by computing the average electric-field intensity on a plane at a fixed sub-wavelength distance above the top of the NPs (15 nm, corresponding to the middle plane of the light-emitting layer in the experimental samples) as a function of illumination angle θ, in the presence of an x-polarized incident plane wave. By reciprocity, the resulting trace is proportional to the x-polarized far-field radiation pattern of a continuous distribution of incoherent electric dipole emitters on the same plane. This procedure has been used to optimize the design parameters of all GMSs of Table 1. The full radiation pattern produced by each optimized GMS (output power as a function of both polar and azimuthal angles) is then calculated through multiple simulations of 3D structures consisting of 20 unit cells of the same GMS, with PMLs on all boundaries. In each simulation, the emitted light is provided by an electric dipole source oriented along the x-, y-, or z-direction, located at different near-field positions where the electric-field-intensity computed in the aforementioned 2D simulations is particularly high (2 to 3 such positions are selected for each GMS design). The field-intensity spatial profile of a representative design is presented in the Supporting Information to illustrate the locations of the selected spots. By reciprocity, in the presence of a continuous distribution, the dipole sources at these positions can be expected to provide the strongest contribution to the output light. In each simulation, the radiation pattern in the air above the device is computed with a far-field projection, and the results for each GMS design are finally added incoherently to one another.

Device Fabrication: The experimental samples are fabricated on Si/SiO_2 substrates. A 100-nm-thick Au reflection layer is first introduced using electron-beam evaporation, followed by a 30-nm-thick SiO_2 film deposited by PECVD. The Au NPs are fabricated by electron-beam lithography with a ZEP resist (ZEP520A, diluted 1:1 in anisole). A 2-nm-thick Au film deposited on the patterned resist by sputtering is used as the adhesion layer in these NPs, to avoid any performance degradation due to the additional losses introduced by other materials commonly used for the same purpose, such as Ti or Cr. The NP fabrication is then completed with the electron-beam evaporation of a 28-nm-thick Au film followed by a lift-off process. Next, spin coating is used to deposit a 30-nm-thick PMMA planarization layer on the NP array, followed by a 30-nm-thick film containing the light-emitting QDs suspended in PLMA. To prepare the PLMA/QD composite films, 100 µL of CdTe/ZnS QDs (Qdot 800 ITK Organic Quantum Dots, ThermoFisher)[38] are suspended in hexane, mixed with ethanol, and centrifuged at 15 000 rpm for 7 min. After centrifugation, the supernatant is drained and 200 µL of diluted PLMA (25 wt. % in toluene,

MilliporeSigma) is added. PLMA includes a long hydrocarbon side chain and its hydrophobic moiety interdigitates with the organic coating on the QDs surface. As a result, it is a particularly well-suited host material to ensure that the QDs are well dispersed rather than forming small clusters. Finally, the devices are capped with an optically thick (≈10 µm) PMMA layer through repeated spin-coating cycles.

Device Characterization: The photoluminescence measurements are carried out with a custom-built optical setup, where the device is pumped with a diode laser at 405-nm wavelength (within the QD absorption band[38]). The collimated beam of laser light is focused on the device by a microscope objective (CF IC EPI Plan 100X, WD 0.30) with a numerical aperture of 0.95. The device photoluminescence is collected with the same objective and its back-focal-plane image (corresponding to the far-field radiation pattern) is recorded with a CMOS camera using a 4-f imaging system. The optical path before the camera also includes a filter with 40-nm-bandwidth pass-band centered at 800 nm, and a beam splitter aligned to another microscope system which is used to image the device during the measurements. A linear polarizer is also inserted in the setup for the polarization-resolved measurements.

Conflict of Interest

The authors declare no conflict of interest.

[1] W. L. Barnes, *J. Mod. Opt.* **1998**, *45*, 661.
[2] J. M. Gérard, B. Sermage, B. Gayral, B. Legrand, E. Costard, V. Thierry-Mieg, *Phys. Rev. Lett.* **1998**, *81*, 1110.
[3] S. Noda, M. Fujita, T. Asano, *Nat. Photonics* **2007**, *1*, 449.
[4] J.-H. Song, T. Atay, S. Shi, H. Urabe, A. V. Nurmikko, *Nano Lett.* **2005**, *5*, 1557.
[5] P. Anger, P. Bharadwaj, L. Novotny, *Phys. Rev. Lett.* **2006**, *96*, 113002.
[6] S. Kühn, U. Håkanson, L. Rogobete, V. Sandoghdar, *Phys. Rev. Lett.* **2006**, *97*, 017402.

**ADVANCED
SCIENCE NEWS**

www.advancedsciencenews.com

**ADVANCED
OPTICAL
MATERIALS**

www.advopticalmat.de

[7] J. S. Biteen, L. A. Sweatlock, H. Mertens, N. S. Lewis, A. Polman, H. A. Atwater, *J. Phys. Chem. C* **2007**, *111*, 13372.

[8] F. Tam, G. P. Goodrich, B. R. Johnson, N. J. Halas, *Nano Lett.* **2007**, *7*, 496.

[9] J. Henson, E. Dimakis, J. DiMaria, R. Li, S. Minissale, L. D. Negro, T. D. Moustakas, R. Paiella, *Opt. Express* **2010**, *18*, 21322.

[10] T. B. Hoang, G. M. Akselrod, C. Argyropoulos, J. Huang, D. R. Smith, M. H. Mikkelsen, *Nat. Commun.* **2015**, *6*, 7788.

[11] I. Staude, V. V. Khardikov, N. T. Fofang, S. Liu, M. Decker, D. N. Neshev, T. S. Luk, I. Brener, Y. S. Kivshar, *ACS Photonics* **2015**, *2*, 172.

[12] M. Caldarola, P. Albella, E. Cortés, M. Rahmani, T. Roschuk, G. Grinblat, R. F. Oulton, A. V. Bragas, S. A. Maier, *Nat. Commun.* **2015**, *6*, 7915.

[13] R. Regmi, J. Berthelot, P. M. Winkler, M. Mivelle, J. Proust, F. Bedu, I. Ozerov, T. Begou, J. Lumeau, H. Rigneault, M. F. García-Parajó, S. Bidault, J. Wenger, N. Bonod, *Nano Lett.* **2016**, *16*, 5143.

[14] D. Bouchet, M. Mivelle, J. Proust, B. Gallas, I. Ozerov, M. F. Garcia-Parajo, A. Gulinatti, I. Rech, Y. De Wilde, N. Bonod, V. Krachmalnicoff, S. Bidault, *Phys. Rev. Appl.* **2016**, *6*, 064016.

[15] V. Rutckaia, F. Heyroth, A. Novikov, M. Shaleev, M. Petrov, J. Schilling, *Nano Lett.* **2017**, *17*, 6886.

[16] A. Vaskin, R. Kolkowski, A. F. Koenderink, I. Staude, *Nanophotonics* **2019**, *8*, 1151.

[17] J. Trevino, H. Cao, L. Dal Negro, *Nano Lett.* **2011**, *11*, 2008.

[18] A. G. Curto, G. Volpe, T. H. Taminiau, M. P. Kreuzer, R. Quidant, N. F. van Hulst, *Science* **2010**, *329*, 930.

[19] H. Aouani, O. Mahboub, N. Bonod, E. Devaux, E. Popov, H. Rigneault, T. W. Ebbesen, J. Wenger, *Nano Lett.* **2011**, *11*, 637.

[20] Y. C. Jun, K. C. Y. Huang, M. L. Brongersma, *Nat. Commun.* **2011**, *2*, 283.

[21] A. E. Krasnok, P. A. Belov, A. E. Miroshnichenko, A. I. Kuznetsov, B. S. Luk'yanchuk, Y. S. Kivshar, *Progress in Compact Antennas*, IntechOpen, London **2014**, Ch. 6.

[22] M. Boroditsky, R. Vrijen, R. Coccioli, R. Bhat, E. Yablonovitch, *J. Lightwave Technol.* **1999**, *17*, 2096.

[23] J. J. Wierer, A. David, M. M. Megens, *Nat. Photonics* **2009**, *3*, 163.

[24] Y. Kurosaka, S. Iwahashi, Y. Liang, K. Sakai, E. Miyai, W. Kunishi, D. Ohnishi, S. Noda, *Nat. Photonics* **2010**, *4*, 447.

[25] A. Vaskin, J. Bohn, K. E. Chong, T. Bucher, M. Zilk, D.-Y. Choi, D. N. Neshev, Y. S. Kivshar, T. Pertsch, I. Staude, *ACS Photonics* **2018**, *5*, 1359.

[26] J. Cesario, M. U. Gonzalez, S. Cheylan, W. L. Barnes, S. Enoch, R. Quidant, *Opt. Express* **2007**, *15*, 10533.

[27] V. Giannini, G. Vecchi, J. Gómez Rivas, *Phys. Rev. Lett.* **2010**, *105*, 266801.

[28] G. Lozano, D. J. Louwers, S. R. K. Rodríguez, S. Murai, O. T. A. Jansen, M. A. Verschuuren, J. Gómez Rivas, *Light: Sci. Appl.* **2013**, *2*, e66.

[29] J. DiMaria, E. Dimakis, T. D. Moustakas, R. Paiella, *Appl. Phys. Lett.* **2013**, *103*, 251108.

[30] L. Langguth, A. H. Schokker, K. Guo, A. F. Koenderink, *Phys. Rev. B* **2015**, *92*, 205401.

[31] N. Yu, F. Capasso, *Nat. Mater.* **2014**, *13*, 139.

[32] P. Lalanne, P. Chavel, *Laser Photonics Rev.* **2017**, *11*, 1600295.

[33] P. Genevet, F. Capasso, F. Aieta, M. Khorasaninejad, R. Devlin, *Optica* **2017**, *4*, 139.

[34] F. Ding, A. Pors, S. I. Bozhevolnyi, *Rep. Prog. Phys.* **2018**, *81*, 026401.

[35] L. C. Kogos, R. Paiella, *ACS Photonics* **2016**, *3*, 243.

[36] S. Sun, K.-Y. Yang, C.-M. Wang, T.-K. Juan, W. T. Chen, C. Y. Liao, Q. He, S. Xiao, W.-T. Kung, G.-Y. Guo, L. Zhou, D. P. Tsai, *Nano Lett.* **2012**, *12*, 6223.

[37] A. Pors, M. G. Nielsen, T. Bernardin, J.-C. Weeber, S. I. Bozhevolnyi, *Light: Sci. Appl.* **2014**, *3*, e197.

[38] www.thermofisher.com/order/catalog/product/Q21771MP (accessed: November 2019).

[39] M. A. Lieb, J. M. Zavislan, L. Novotny, *J. Opt. Soc. Am. B* **2004**, *21*, 1210.

[40] E. Khaidarov, Z. Liu, R. Paniagua-Dominguez, S. T. Ha, V. Valuckas, X. Liang, Y. Akimov, P. Bai, C. E. Png, H. V. Demir, A. I. Kuznetsov, *Laser Photonics Rev.* **2019**, *14*, 1900235.